

Two-dimensional mapping of falling water film thickness with near-infrared attenuation

J. Dupont^{1,2} · G. Mignot¹ · H.-M. Prasser^{1,2}

Received: 2 July 2014 / Revised: 28 March 2015 / Accepted: 2 April 2015 / Published online: 21 April 2015
© Springer-Verlag Berlin Heidelberg 2015

Abstract We have developed an optical technique for the two-dimensional mapping of water film thickness. The technique is based on infrared light absorption. A near-infrared camera is used to capture the radiation returning from a surface illuminated by a halogen lamp. The attenuation of the back-scattered radiation is used as a measure for the thickness of the water film covering the surface. The method was calibrated using well-defined liquid films between a glass plate and the surface. Series of instantaneous, two-dimensional thickness profiles of wavy turbulent free-falling films along a vertical wall were measured at a frame rate of 200 Hz. The evolution of complex flow patterns with three-dimensional instabilities such as long waves and capillary waves was observed under isothermal conditions. For the validation of the method, simultaneous independent measurements were taken together with an electrical high-speed liquid film sensor.

1 Introduction

Measurement of the liquid film thickness has been an important topic in the area of two-phase flows. Water films are present in many industrial processes where their understanding is of relevance regarding process optimization and safety evaluation (de la Rosa et al. 2009; Anderson et al. 1998; Malet et al. 2005; Doniec 1988; Ambrosini et al. 2002; Huang and Cheng 2014). Among the numerous experimental methods allowing for the thickness

measurement of liquid films, one may distinguish five different working principles listed in Table 1 (an extended version of the Collier and Hewitt's scheme (Clark 2002a).

In terms of thickness range, there is no physical but practical limitations for the methods *a* to *f* where the minimal and maximal measurable thicknesses depend on the sizing of the experimental setup and the accuracy of the detection. The methods *g* to *o* show a limitation due to increasing attenuation in the media with the thickness. Interferometry and pulse-echo have a lower limit which is proportional to the wavelength. Only interferometry shows an upper limit which is associated with a multiple of the wavelength.


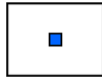
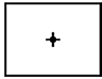
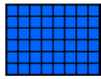
Few methods were applied for the spatial measurement of the film thickness. A conductance technique with multiple electrodes was introduced by Belt et al. (2007, 2010). A similar technique was used by da Silva et al. for mapping gravity-driven mixing processes in a pool (da Silva et al. 2007) and for the detection of the gas–liquid interface in a hydraulic coupling; a hydrodynamic device used to transmit rotating mechanical power (da Silva et al. 2008). Damsohn and Prasser (2009) developed an electrical liquid film sensor (LFS) with an improved spatial resolution compared with Belt et al. and Silva et al. The LFS has been extensively used for the study of annular flows, which are characterized by the presence of a liquid film, driven by a gas flow, progressing on the inner wall of a channel. The sensor is mounted flush to the surface and is thus non-intrusive as long as the liquid film covers the surface completely. The formation and propagation of contact lines on partially wetted surfaces, however, may be affected by the wettability of conducting electrodes and insulating areas. In the case of capacitance probes, such as those discussed by Ambrosini et al. (2002), both electrodes and insulating areas can be covered with the same material as for the entire surface, which eliminates this deficiency.

✉ J. Dupont
julien.dupont@psi.ch

¹ Paul Scherrer Institut (PSI), Villigen, Switzerland

² ETHZ, Zurich, Switzerland

Table 1 Working principles and an extended version of the Collier and Hewitt's scheme of film thickness measurement techniques [adapted from Clark (2002a), Damsohn and Prasser (2009)]

Working principle	Method	Collier and Hewitt classification			
		Average	Local	Point	Spatial
					
Mechanical	(a) Extraction/weighting	✓			
Electrical	(b) Needle contact probe			✓	✓
	(c) Conductance	✓	✓	✓	✓
	(d) Capacitance		✓		✓
Photon	(e) Shadow			✓	
	(f) Confocal/laser focus displacement			✓	
	(g) Optical fiber			✓	
	(h) Visible light absorption			✓	✓
	(i) X-ray absorption			✓	✓
	(j) Luminescence			✓	✓
	(k) Laser scattering			✓	
	(l) Interferometry			✓	
	(m) Total internal reflection			✓	
Neutron	(n) Neutron absorption		✓		✓
Ultrasound	(o) Pulse-echo		✓		✓

Both conductance and capacitance methods show a mutual dependence between the measurable thickness range and the spatial resolution. This dependence is attributed to the geometry of the electrical field covering the volume of interest where two-phase flow is observed. Kang and Kim (1992) found that a flush-wire probe offers higher spatial resolution for an extended thickness range at the cost of an intrusive wire inserted into the film.

Optical techniques such as luminescence and light absorption in the visible range require the doping of the liquid film with agents necessary for the appropriate contrast (Clark 2002a; Alekseenko et al. 2008; Clegg 1969). Additives may turn out to be surface-active substances, affecting the surface wettability by changing the contact angle. In a similar way, the application of seeding particles is also problematic. Light emission through fluorescence or light scattering such as Rayleigh or Raman scattering (Greszik et al. 2011) with pure water shows very weak intensities for a given illumination strength and is thus not practical. Interferometry of light emitted through blackbody radiation was exploited by Dumin (1967) to measure the thickness of a growing silicon layer on a sapphire substrate. In this case, the high temperature of the process (1100 °C) provides sufficient thermal radiation for detection in a spectral band ranging from 1.7 to 2.7 μm .

Ultra-fast X-ray radiography and tomography (Hampel et al. 2005; Fischer and Hampel 2010) were used to perform time-resolved two-phase flow measurements [up to

10 kfps with a spatial resolution of 1 mm (Bieberle et al. 2010)], but it fails when the test section is made of absorbent materials. Also, X-ray measurements require good accessibility for the radiation source placed in the vicinity of the test section. Imaging with thermal and in particular cold neutrons is highly sensitive to water thanks to the high attenuation, by elastic scattering and radiative capture, of the hydrogen atom. However, measurements are often limited by relatively low neutron fluxes which result in a time resolution of a few Hz in the best cases. Also, the generation of strong neutron beams requires large-scale facilities (Kickhofel et al. 2011).

Ultrasonic pulse-echo techniques were investigated by Kamei and Serizawa (1998) for a fuel rod geometry and by Chen et al. (2005) for a planar geometry with condensation. Kamei performed spatial ultrasonic measurements of the liquid film thickness on the surface of a fuel rod simulator. In a nuclear boiling water reactor, the coolant flows along cylindrical fuel rods and continuously evaporates while the flow structure approaches the regime of annular flow. Measurements of the film thickness in this flow regime were taken in a scanning mode with 40 measuring positions and a frame rate of 250 fps. Chen used eight transducers in parallel for a measuring frequency of up to 30 Hz. Despite the fact that ultrasounds are non-intrusive, their relatively large wavelength limits the measurement accuracy for thin films to the order of a few hundred micrometers. The main drawbacks are the

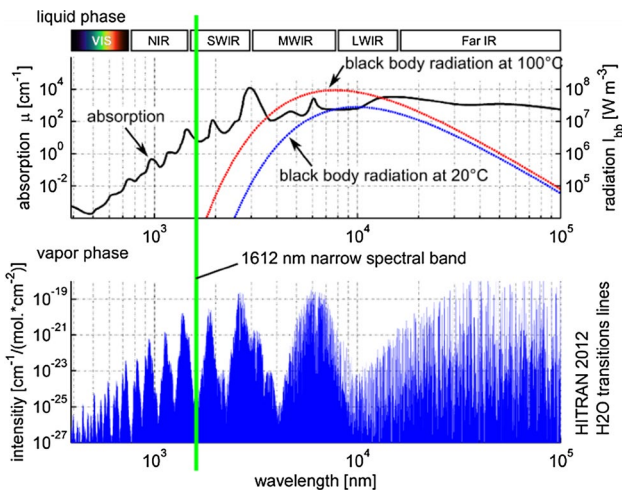


Fig. 1 Optical properties of liquid water (*top*) and water vapor (*bottom*), from Segelstein (1981), The HITRAN 2012 (2013)

limited spatial resolution when using multiple transducers and receivers for 2D imaging and combining high time resolution with a large number of measuring points in the scanning mode.

With regard to light attenuation, liquid water has a complex absorption spectrum which shows strong variation in the infrared as pictured in Fig. 1. This allows optimizing the attenuation for a desired film thickness range by picking a suitable wavelength. Brissinger et al. (2014) used a laser beam centered at 1638 nm to follow the film thickness evolution of a free-falling film on a ZnSe window. Corkill et al. (1963) measured the water content of black foam films (‘black films’ are liquid films stabilized by a surfactant, which have a thickness smaller than the wavelength of visible light, which renders them invisible) by observing a beam attenuation at 2930 nm where an absorption maximum for water is found. Debrégeas et al. (1995) reported the thickening of viscous bursting freely suspended films by measuring the attenuation of a 0.5-mm-diameter infrared beam. Numerous similar measurements can be found elsewhere (Yang et al. 2010, 2011; Wittig et al. 1992; Sattelmayer 1987) where windows were made of glass or quartz. In each case, different wavelengths have been investigated to achieve an adequate absorption coefficient according to the thickness range under investigation. All the mentioned applications were local transmission measurements in a single sensitive region defined by the applied light beam.

Water exhibits very low attenuation in the visible wavelengths. A film thickness measurement by attenuation in the visible requires the addition of a water-soluble dye to enhance the film absorption. This was first used for a 2D thickness mapping of a liquid film on a glass plate by Clegg (1969) with photographic plates and three decades later by Clark (2002b) with a digital camera. Both

authors report the use of a light diffuser placed between the light source and the film with the camera placed on the opposite side such that light passes through the transparent wall.

Our contribution consists in combining 2D camera imaging with the application of near-infrared (NIR) light in a narrow wavelength band for a time-resolved water film thickness mapping on a non-transparent wall by taking advantage of the diffuse reflection of the wall surface. The light source and camera are located next to each other on the same side of the observed surface. For the validation of the method, simultaneous independent measurements were taken together with the LFS of Damsohn et al.

2 Working principle

2.1 Measuring setup

Figure 2 shows a schematic of the measuring setup with the light source, the water film on the surface of a diffusely reflecting, non-transparent wall and the NIR camera. Each pixel of the camera sensor corresponds to one optical path carrying information related to a location in a 2D measuring domain on the observed surface. The photons are emitted from the light source and directed toward the camera’s field of view (FOV) on the surface. A narrowband filter selects photons of the chosen wavelength. The filter can be placed either in front of the light source or in front of the camera. The light that is recorded by the camera passes twice through the water film. Therefore, the attenuation corresponds to the absorption of twice the thickness of the water film. Reflection and refraction occurring on the liquid surface at the interface between the liquid and air must be taken into account when interpreting the intensity recorded by the camera.

We selected a wavelength of 1612 nm corresponding to an absorption coefficient of 7.2 cm^{-1} @ 22 °C (Kou et al. 1993). This guarantees a minimum transmission of about

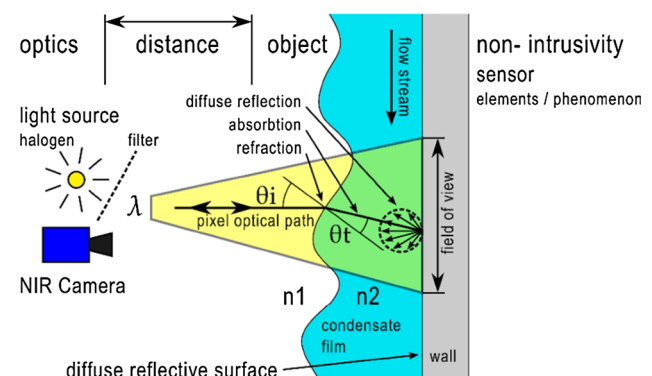


Fig. 2 Scheme of the measurement principle

5 % in case of a maximum film thickness of 2 mm (Ambrosini et al. 2002; Ozler Emrah Talip 2007), which was chosen as the upper limit of the measuring range. As shown in Fig. 1, the selected wavelength corresponds to a minimum of absorption in the steam phase such that transmission losses in air due to the presence of humidity are minimized. For liquid water at room temperature, blackbody radiation in the NIR is too weak to be detected and does thus not interfere with the film thickness measurement.

Most absorption methods rely on unidirectional light transmission through a film on a transparent wall or through a free liquid film. We propose instead to illuminate a wall from the wetted side and measure the reflected intensity. In this way, a water film on an opaque wall can be studied. The wall could therefore be covered with different non-transparent coatings. The method is best suited for surfaces with a diffuse reflection.

2.2 Signal processing

The light intensity recorded by a single pixel of the infrared camera is converted into a local instantaneous water film thickness using the assumption of a planar film on a surface that is perpendicular to both the incoming light beam and the optical axis of the camera. Since the light traverses twice through the film, Beer–Lambert law connects the measured intensity I and thickness x as follows:

$$I = I_0 \cdot \exp(-2\mu x) \quad (1)$$

Here, I_0 is a reference intensity valid for a film thickness converging to zero, and μ is the attenuation coefficient of water in the wavelength range selected by the narrowband filter. Both I_0 and μ are determined by calibration. The value of I_0 includes the reflective properties of the surface as well as contributions to the attenuation by partial reflection from the air–water interface.

From the literature (Twomey et al. 1986; Xu et al. 2003; Wolff 1994), it is known that dry and wet surfaces have different reflective properties. The constant factor, I_0 , in Eq. (1) has to correspond to the case of a wet surface. We introduce the correction factor K_{dry} in order to relate the intensity of the radiation received by the camera from a wet surface covered by a very thin liquid film to the intensity returning from a dry surface such that,

$$K_{\text{dry}} = \frac{I_0}{I_{\text{dry}}} \quad (2)$$

The intensity I_{dry} can be directly measured during calibration, while I_0 has to be obtained by fitting intensities measured at different liquid film thickness values, using Beer–Lambert's law. A detailed derivation of the signal processing is given in Appendix 2.

3 Experimental setup

3.1 Camera and lens specifications

A FLIR (forward looking infrared) SC2500 NIR camera was used for the purpose of this work. The model features a 256×320 pixels InGaAs detector array sensitive to a spectral band ranging from 900 to 1700 nm with a peak quantum efficiency $\eta_{Q,\text{max}}$ above 70 % at 1500 nm. With a pixel pitch of $30 \mu\text{m}$ and a fill factor equal to 100 %, the detector size is equal to 9.60×7.68 mm. The camera is capable of acquiring images at rates up to 340 fps for full frame and up to 15 kfps when windowing (128×8 pixels) is applied. A minimum integration time of 400 ns is achievable. The analog-to-digital converter provides 14-bit output data ensuring good counting statistics. With this type of detector, nonlinear correction of the signal is not required. The camera's lens has a focal length $f = 50$ mm and a relative aperture $f/2$. The imaging setup delivers a FOV of approximately $153.6 \text{ mm} \times 192 \text{ mm}$ and a projected pixel size of approximately 0.6 mm/pixel when placed at 1 m from the object. Between the lens and the detector, a slot mounted on the camera allows for the insertion of spectral filters made necessary due to the polychromatic light source. For the purpose of thin film measurements, a narrowband filter centered at 1612 nm with a bandwidth of 32 nm was used.

3.2 Optical assembly with a light source

Two options for the light source were compared: (1) pulsed infrared laser diodes and (2) a halogen lamp combined with a narrowband filter. The halogen source combined with the light projection system, as described in Fig. 3, was chosen because of the higher output. The halogen bulb emits blackbody radiation characterized by a broad emission spectrum. Thus, the intensity loss due to the narrowband filter is significant. Further losses occurring during the collection of light and its projection on the wall were considered. Approximately, the filter reduces the total intensity by a factor of 100, and another reduction factor of 10 is attributed to the collection efficiency of

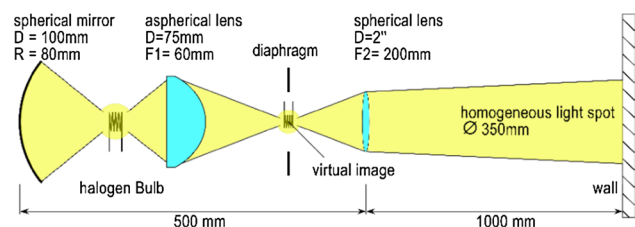


Fig. 3 Scheme of the light source with optical elements

the light projection system. Finally, the required electrical power for sufficient illumination was found to be on the order of 100 W. Details of the above estimations are given in Appendix 1. We used an industrial halogen bulb with a maximum power of 1000 W, and a color temperature of 3200 K when 220 V is supplied. We lowered the applied voltage to optimize the light output and to lower the color temperature such that the maximum of the Planck spectrum is shifted closer to the detection band. For the measurements on the gold-covered surface of the LFS described below, a voltage of 40 V corresponding to a power of 66 W was necessary to obtain between 80 and 90 % of detector saturation when imaging the dry surface, which confirms the order of magnitude predicted by the calculation in Appendix 1. According to Wien's displacement law, the corresponding emission maximum of the bulb at this voltage and power is at 1787 nm, which is close to the bandpass of the filter.

Figure 3 shows a schematic of the alignment of the main optical components used in the light projection system. N-BK7 lenses and a protected aluminum mirror were used for their good transmission and reflection values, respectively.

A spherical mirror and an aspherical condenser lens placed on opposite sides of the bulb collect the light. A diaphragm acts as a second means of light output control. Behind the virtual image, a spherical projection lens conditions the beam to ensure a homogenous illumination with the desired opening angle. It is difficult to arrange light source and camera exactly on the same optical axis. This would require coupling of forward and backward beams by a semitransparent mirror, an idea which was abandoned for practical reasons. In our case, lamp and camera are placed closely side by side as shown in Fig. 4. The distance between the centers of the two front lenses is 95 mm.

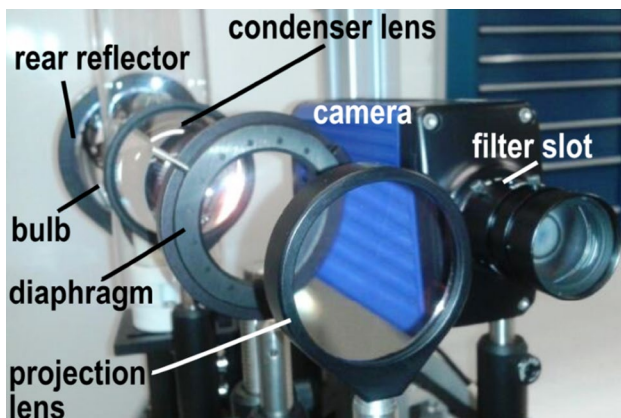


Fig. 4 Photograph of the optical setup

4 Test procedure

4.1 Validation with the liquid film sensor

An independent validation of the NIR film thickness mapping was carried out by comparison with the electrical LFS described in (Damsohn and Prasser 2009). The sensor consists of a two-dimensional matrix of electrodes with a pitch of 2 mm in both directions. The LFS is built on a flat printed circuit board where transmitting and receiving electrodes are mounted flush to the surface. The sensor plate formed the wall surface in the experiments. It was placed vertically in front of the optical system at a distance of about 1 m from the camera. The electrical sensor measures the film thickness in a range of up to 800 μm on a matrix of 16 points horizontally and 64 points in the vertical direction.

For the validation test, a water film was generated by spreading tap water onto the upper part of the sensor above its sensitive area (i.e., the area covered by electrodes). The falling film on the sensor surface was isothermal. A constant flow rate was applied during the entire measurement. The film thickness was measured in parallel with both NIR and the LFS techniques. A TTL connection was made between the camera and the LFS to synchronize data acquisition.

4.2 Correction of fluctuations of the illumination intensity

The light intensity returning from the measured object is affected by fluctuations of the lamp power and temperature, as well as by changes in the attenuation in the atmosphere along the optical path. For the compensation of these influences, a reference intensity was recorded by evaluating the light intensity returning from a small area of surface outside the region covered by the liquid film. An identical reference surface was used during both calibration and measurement. In the experiments presented here, the surface was white paper and placed left from the side edge of the LFS wetted surface, at the same distance from the camera, and within its FOV as shown in Fig. 5a. The LFS surface did not cover the entire width of the FOV such that enough space was left on the sides, in the extension of the surface, for a reference surface. The reflected intensity from the reference surface is recorded together with the information from the water film. Since the reference surface is not covered by liquid, its reflective properties remain constant. The intensities of all obtained images were normalized by the average signal over a region of interest of 11×55 pixels on the reference surface before the further data processing steps were taken. As a consequence, relative measurements are taken thereby cancelling out uncertainties due to fluctuations in

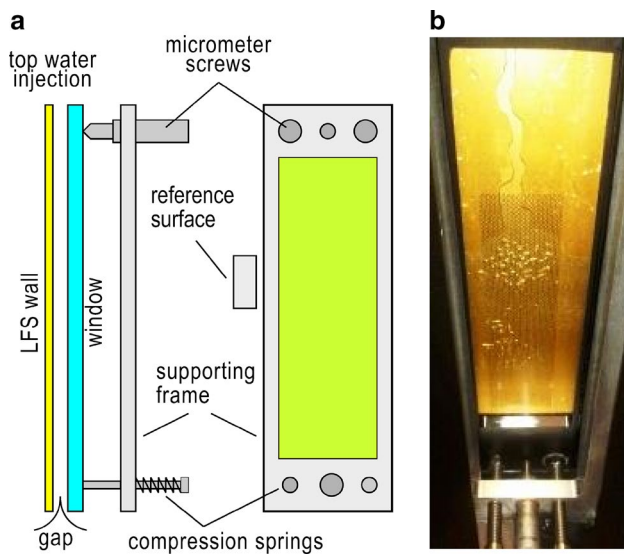


Fig. 5 Calibration setup: **a** side and front-facing view of the setup with reference surface, **b** front-facing picture showing water partially filling the gap

absorption in the air, lenses or a window, changes in the quantum efficiency of the detector and variation in the illumination intensity. The intensity, i , related to the reference intensity is derived in Appendix 2.

4.3 Calibration

The LFS was calibrated independently using the dynamic roll technique as described by Damsohn (2011). A calibration tool dedicated to the NIR imaging technique was designed, which can be used with the LFS as well as with other types of surfaces. It consists of a borosilicate window driven by 3 micrometer screws which is held in a metallic frame fixed to the LFS. A precise positioning of the window with reference to the surface ensures a uniform gap between the window and the LFS surface over the whole area of measurement while allowing optical access as shown in Fig. 5.

While the gap was completely filled with continuously flowing tap water, a measurement was recorded as described in Sect. 4.4. Each measurement was repeated 2 to 3 times for each film thickness. The procedure was repeated for various thicknesses ranging from 100 to 2100 μm in steps of 100 μm . An additional measurement with a dry surface $i_{\text{dry,calib}}$ was performed. To compensate the effects of the window, the corrected dry measurement $i_{\text{dry,calib,corr}}$ was calculated as follows,

$$i_{\text{calib,dry,corr}} = i_{\text{calib,dry}} \frac{L_{R,a \rightarrow g} \cdot L_{R,a \rightarrow w}}{L_{R,g \rightarrow w}} \quad (3)$$

where $L_{R,x \rightarrow y}$ is reflection losses at an interface between medium x and medium y . The indices a , g and w stand for

the air, glass and water mediums, respectively. The parameter i denotes the intensity normalized by the reference measurement. We measured the refraction index of the glass used in order to calculate $i_{\text{calib,dry,corr}}$. The full derivation of Eq. (3) can be found in Appendix 2.

For film thickness measurements, only the window was removed from the calibration setup. The characteristics and position of all elements including the reference surface remained unchanged. However, according to Appendix 2, the calibration can also be performed ex situ with a sample of the test surface and a different reference surface.

4.4 Data processing

For all measurements, frames were acquired at a frequency of 200 Hz for 10 s resulting in a total of 2000 frames. The exposure time of the camera was set to 500 μs to avoid motion blurring.

The explicit expression for the film thickness according to Eqs. (1–2) and to Appendix 2 is written as follows.

$$x = \frac{1}{2\mu} \left(\ln(K_{\text{dry}}) - \ln\left(\frac{i}{i_{\text{dry}}} - c\right) \right) \quad (4)$$

A constant c was added to characterize the background illumination which makes thick films appear not completely black. The calibration points were fitted with Eq. (4) in order to obtain the coefficients μ , K_{dry} and c . Determining the liquid film thickness consists in solving Eq. (4) for all measurement points in the FOV.

In addition, the following corrections and processing steps were performed:

Offset correction The dark current was recorded immediately after each measurement with the light source switched off while keeping the same integration time (i.e., 500 μs). A total of 2000 dark frames were averaged and subtracted from each measurement frame. The dark current varies with the temperature of the detector. However, temperature changes in the detector are expected to be negligible in the short time between the measurement and the dark current acquisition.

Dry surface measurement When images of the dry surface are acquired, time averaging is performed to reduce background noise. Since the dry surface measurement results in the largest light intensity, it was used to adjust the power of the light source to achieve good utilization of the dynamic range of the camera.

Calibration measurements During calibration measurements, small air bubbles were sometimes observed within

the flow. A temporal median filter was applied in order to eliminate artefacts caused by bubbles.

5 Results and discussion

5.1 Calibration

The transmission as a function of the film thickness obtained from the calibration is plotted in Fig. 6. Average values were taken over the area of the LFS covered by electrodes. The values were normalized by the corrected dry surface intensity $i_{\text{dry,cal,corr}}$ (see Sect. 4.3) which was set to 1, i.e., 100 % transmission. Since the intensities are temporal and spatial averages, the error bars correspond to the uncertainty according to relative measurements with a reference surface as discussed in Sect. 5.3. The micrometer screws have an error of $\pm 5 \mu\text{m}$.

The calibration points, the curve fit, its corresponding equation and coefficients are shown in Fig. 6. The separately plotted intensities $i_{\text{dry,cal}}$ and $i_{\text{dry,cal,corr}}$ were not included in the fit. The correction factor, K_{dry} , corresponds to the proportional factor ‘ a ’ in the fitting equation and was found to be equal to $81.0 \pm 0.17 \%$. The value of K_{dry} depends on the optical properties of the surface. Thus, for future applications it should be noted that each type of surface requires its own calibration.

The exponential decay constant was found to be $14.8 \pm 0.1 \text{ cm}^{-1}$ corresponding to an absorption coefficient μ equal to 7.39 cm^{-1} . This is very close to the absorption coefficient found in the literature for a wavelength of 1612 nm (Segelstein 1981; Wieliczka et al. 1989; Kou et al. 1993), which is reported to lie between 6.56 and 7.20 cm^{-1} .

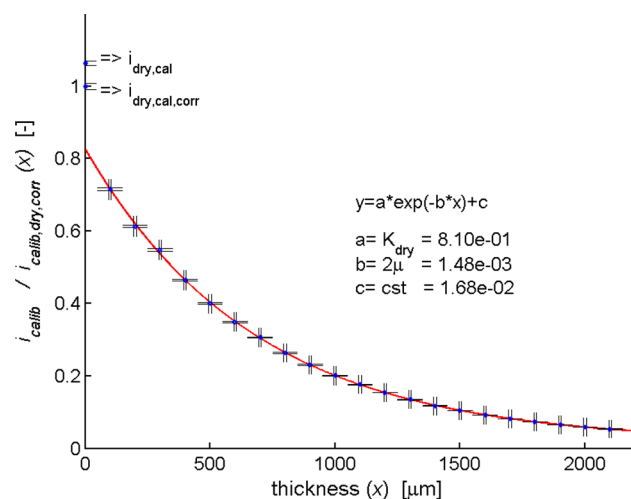


Fig. 6 Calibration curve and corrected dry surface intensity with error bars

Discrepancies are partially due to uncertainties in the water temperature and the filtered wavelength. In our case, the observed bias toward more absorption is the result of changes in the angle of incidence of the optical path over the FOV as shown in Fig. 2, as well as the non-collinear optical axis of light source and camera, and the tilting of the wall surface as discussed in Sect. 5.3. Similarly, as discussed in Appendix 2, internal reflections in the film lead to an overestimation of the product μx . Since measurements were taken under the same conditions as the calibration, the measured absorption coefficient was used for the calculation of the film thickness.

5.2 Test measurements with a wavy turbulent water film

The comparison between the NIR method and the LFS was carried out with a wavy turbulent film generated by spreading water across the upper part of the sensor surface above the sensitive area covered by electrodes. An example of a frame acquired from the NIR camera and the processing steps to obtain an instantaneous 2D mapping of the water film thickness are shown in Fig. 9.

The dry surface (a) and wavy film (b) shown in the figure are relative intensities normalized by the intensity obtained from the reference surface and are thus dimensionless (grayscale between 0 and 1). The pattern formed by the electrodes is clearly visible in (a) and (b). It nearly cancels out when the dimensionless transmittance (c) is calculated as the ratio of (b) divided by (a). The transmittance is also dimensionless and takes values between 0 and 1, as well. Finally, the film thickness is calculated from the transmittance using Eq. (4) and the coefficients obtained from the calibration. The red dashed rectangle inserted in Fig. 7d indicates the area covered by the sensible area of the LFS. From the known size of this area, we found a projected pixel size of 0.61 mm/pixel in the horizontal direction and 0.60 mm/pixel in the vertical direction.

Figure 8 shows simultaneous mappings of the film thickness obtained with the NIR imaging technique (a) and with the LFS (b) over the area depicted in Fig. 7d. The flow pattern is recognizable with both methods and shows an excellent qualitative correspondence in space and time within the limits of the discretization of the LFS. Major flow structures such as solitary waves with large film thickness amplitude are distinguishable with both techniques. Thanks to the higher spatial resolution, the camera perceives capillary waves with a higher spatial frequency occurring between larger waves (Kofman et al. 2014; Yu et al. 2011). Those fine structures are not resolved by the LFS. For a quantitative comparison, the spatial resolution of the imaging technique was reduced to match that of the LFS as shown in Fig. 8c. The down-sampling of the NIR measurement to 16×64 pixels was obtained by averaging

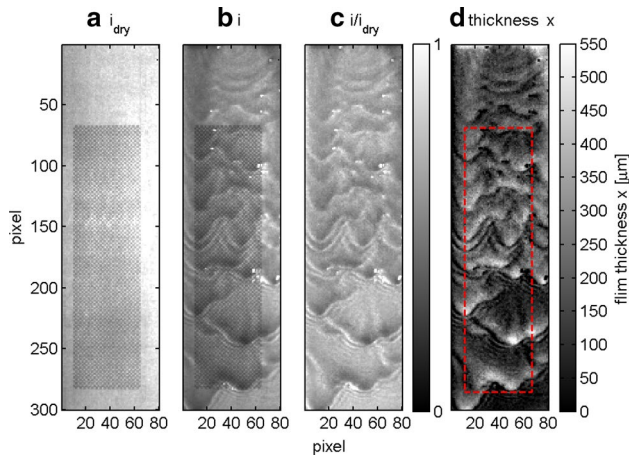


Fig. 7 NIR imaging processing steps: **a** dry surface intensity, **b** transmitted intensity with a falling film, **c** transmittance I/I_{dry} , **d** film thickness mapping

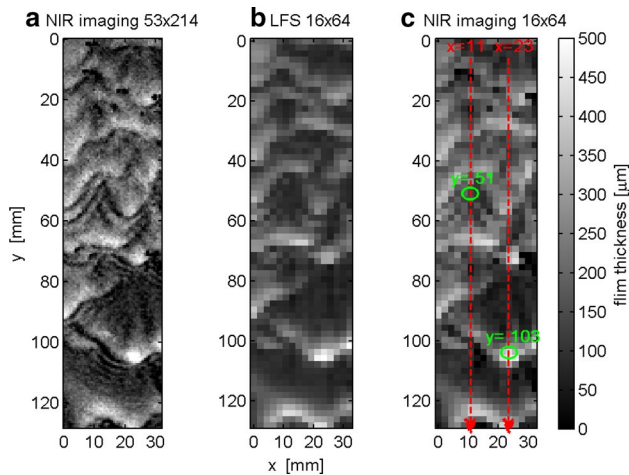


Fig. 8 Qualitative comparison: **a** NIR imaging with full resolution, **b** LFS, **c** NIR imaging with a reduced spatial resolution (16×64) to match the electrode pitch of the LFS

over two-dimensional areas equivalent to the size of 11 pixels of the camera which improves statistically the precision of the measurement and helps to explain the generally good agreement with the LFS. Profiles along both vertical lines depicted in Fig. 8c were compared in Fig. 9. Additionally, film thickness as a function of time was extracted at the two locations marked by green circles in Fig. 8c for comparison as shown in Fig. 10. In both figures, the water film thickness measured by the NIR technique is given in the full camera resolution and in the down-sampled resolution equivalent to the electrode pitch of the LFS. In the full resolution, small flow structures are clearly visible which are absent in the reduced resolution images as well as in the signal of the LFS.

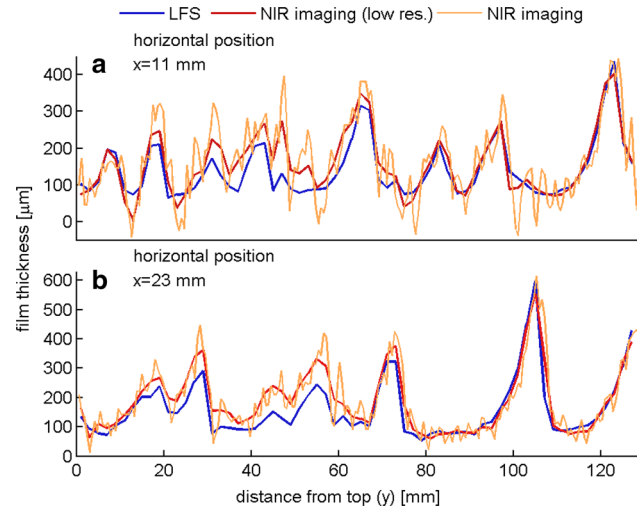


Fig. 9 Instantaneous spatial profiles for quantitative comparison

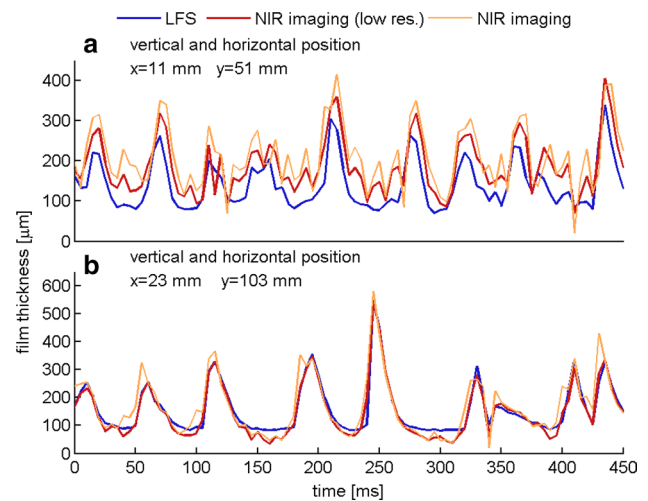


Fig. 10 Comparison of local signals as function of time

As shown in Figs. 7 and 8, the evolution of the flow from top to bottom of the LFS surface is visible. Small waves present in the upper part grow to larger waves with simpler structures by the time they reach the bottom. Between the two regimes, a transition with complex flow structures resulting from wave interferences occurs. Generally, wave crests and troughs, captured independently by both measurement techniques, show remarkably good agreement.

5.3 Discussion of uncertainties

Specular reflections In Sect. 2.2, we assumed a flat film and a normal incident illumination on the surface. In fact, we slightly tilted the surface by 4° with regard to the

direction of the observation in order to avoid that specular reflections from the air–water interface are captured by the camera. This does not totally exclude the occurrence of specular reflections, since the occurrence of waves in the film leads sporadically to an unfavorable local surface tilt. Specular reflections are responsible for the spots of high intensity visible in Fig. 7b, c. Specular reflections exceed the intensity of the dry surface signal, which makes them clearly distinguishable. They bring the camera's detector to saturation and are translated into negative values of the film thickness. At the affected areas, a film thickness measurement is temporarily impossible.

Angle of incidence In case of a flat film, the angle of incidence of an optical path varies between the center of the measurement field where it equals 4° (tilt angle) and the periphery where a maximum and a minimum of 6° and 3° are found. An increasing angle results in larger reflection losses at the film surface, a longer absorption path and less reflection from the wall surface. Using Snell's law and the Fresnel equations, the refraction indexes of air and water, and assuming a Lambertian surface, we calculated the intensity deviation with reference to the center of the measurement field. The maximum film thickness in our measurements is $600\ \mu\text{m}$ for which a maximum intensity deviation is found between 4° and 6° of incidence corresponding to $0.17\ \%$ uncertainty.

For the case of a wavy turbulent film, uncertainties related to the film surface angle have to be considered. Figure 11 depicts the intensity variation as a function of the film surface angle for three different film thicknesses. The corresponding derivations are reported in Appendix 3.

With regard to the surface angle, Fig. 11 can be used for the quantification of the resulting measuring error. The error was checked for an angle of 20° . The corresponding intensity deviation compared to a flat film of $600\ \mu\text{m}$ is equal to $0.71\ \%$. The maximum error related to the angle of incidence of an optical path is thus $0.17\ \% + 0.71\ \% = 0.88\ \%$.

Accuracy of the relative measurement by means of the reference surface The amplitude of fluctuations in the illumination intensity, in the camera's detector temperature and in absorption through the air might vary over the FOV between the locations of the reference surface and the measurement field. To assess the accuracy of a measurement relative to a reference surface, we measured changes in the homogeneity of the detected intensity over the FOV with regard to temperature variations in the detector and variable illumination intensity. These measurements were taken on a dry surface. The time- and spatial-averaged value of a region 30×30 pixels large in the center of the

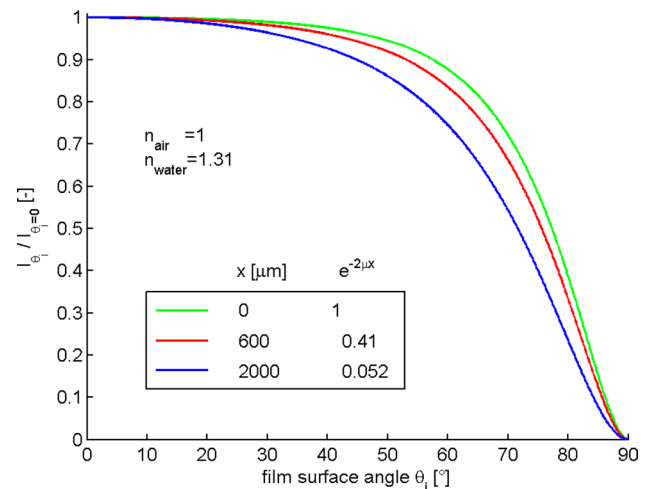


Fig. 11 Reflected intensity versus film surface angle

FOV was compared with the reference surface. The difference between the ratios of the intensities from the two regions was equal to $0.28\ \%$ after a temperature change in the detector of $8\ ^\circ\text{C}$ and to $0.25\ \%$ for an illumination change of $300\ \%$, which is a conservative envelop of the variation in both quantities during our measurements. The fluctuations in air absorption were similar to those in the measurement. Their resulting uncertainty is included in the above measures. A resulting total error corresponding to the sum of uncertainties, i.e., $0.53\ \%$, was attributed to all measurements.

Caustics The curvature of the liquid film surface creates an illumination pattern on the wall surface with intensity variations depending on whether the light is concentrated by focusing or inversely if defocusing occurs. In fact, the reflected light from the surface which is directed backward toward the camera's lens returns from the surface through the same area in the film where it previously entered. As a consequence, the reflected light undergoes the exact inverse of the deflection of the incoming light due to refraction. Thus, the effect of light focusing or defocussing on a curved surface cancels out as shown in Fig. 14.

Involuntary heating of the film The use of an external light source has the effect of heating the liquid film. A derivation of the light strength is given in Appendix 1. According to the detector and lens specifications, the distance from the wall surface and the area of illumination, $0.12\ \text{W}$ continuous illumination intensity I_{illu} is required which corresponds to a radiation flux on the surface of approximately $2\ \text{W m}^{-2}$. In our experiment, the narrowband filter was inserted in the camera between the lens and the detector.

Thus, a broad band spectrum between 300 and 2700 nm was transmitted through the N-BK7 lenses of the light projection system raising the total flux to approximately 92 W m^{-2} .

In order to obtain a conservative estimate for the increase in the film temperature, a liquid film with $Re = 30$, the lower limit for wavy or turbulent films, was assumed. The films in the presented experiments are well above this limit. In the worst case, the radiation is fully absorbed in the liquid, the film is thermally isolated, and the flow rate can be calculated from a laminar film model with the input of the Reynold number $Re = 30$. For water at $20 \text{ }^\circ\text{C}$, the corresponding flow rate $\Gamma_{Re=30} = 7.5 \text{ g m}^{-1} \text{ s}^{-1}$ and the maximum illumination spot diameter of 0.28 m lead to a upper limit of the temperature increase in our film of $0.82 \text{ }^\circ\text{C}$. Note that this result is strongly conservative. The film in the real measurements was turbulent, and the flow rate was thus considerably higher. Furthermore, the liquid film dissipated thermal energy to the environment, which removed a part of the deposited energy.

In other applications where the energy absorbed is not driven away by the flow, such as stationary films or in the presence of dry areas, the temperature elevation might be a concern. In this case, the narrowband filter should instead be placed in front of the light source to reach the above-mentioned lower heat flux of 2 W m^{-2} . We notice that in this case, the heat flux is similar to the one removed by heat transfer due to free convection in air at a driving temperature difference of about 1 K , which is characterized by a heat transfer coefficient of about $2\text{--}10 \text{ W m}^{-2} \text{ K}^{-1}$ (Incropera and DeWitt 1996). Consequently, a maximum temperature elevation should stay below about 1 K in the worst case. Several possibilities exist to further decrease the heat flux such as longer integration times, pulsed illumination and a shorter distance between the optics and the wall.

In general, for each application of the technique the potential for surface heating should be considered with care. To clarify the sensitivity of the absorption coefficient μ to temperature changes, the attenuation in a static water film with constant thickness was measured by varying the temperature between 10.1 and $24.1 \text{ }^\circ\text{C}$. In this temperature range, the normalized absorption coefficient with reference at $20 \text{ }^\circ\text{C}$ shows a relative variation of $0.15 \text{ } \%$ K^{-1} as depicted in Fig. 12. The weak dependence on temperature observed at 1612 nm is in good agreement with the measurements of Yang et al. (2010).

We added an uncertainty of 1 K due to a temperature difference between calibration and measurement to our conservative assessment of the variation in the film temperature of 1 K , due to the heating. Together with the interval of confidence of $0.65 \text{ } \%$ obtained from the calibration, the total error on μ is $0.15 \text{ } \%$ + $0.15 \text{ } \%$ + $0.65 \text{ } \%$ = $0.95 \text{ } \%$.

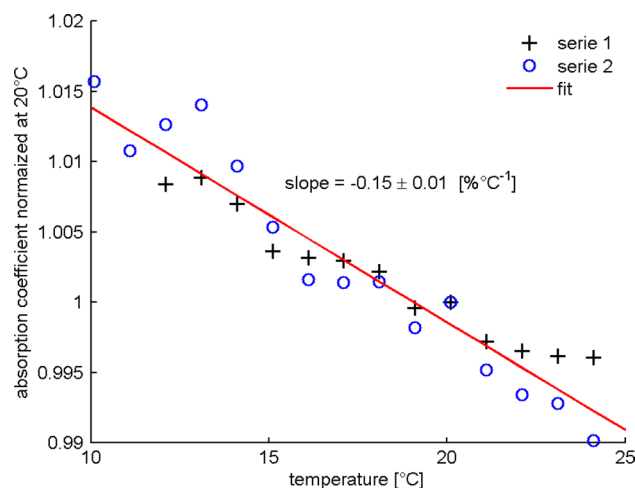


Fig. 12 Relative changes of the water absorption coefficient μ with temperature. Two measurement series for temperatures ranging from 10.1 to $24.1 \text{ }^\circ\text{C}$ are depicted

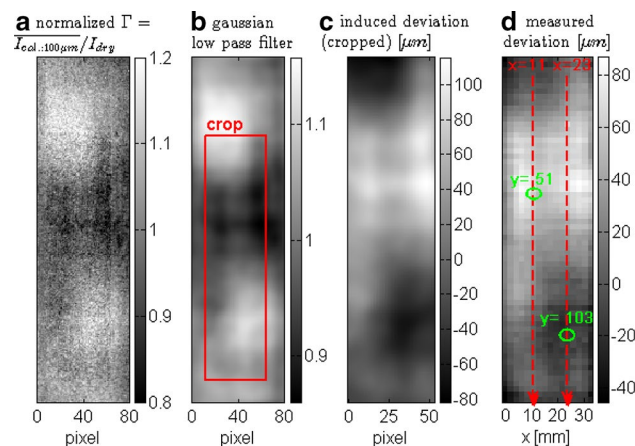


Fig. 13 Estimated offset deviation for NIR imaging and measured deviation with the LFS

Non-homogeneity of K_{dry} Figure 13 shows the variation in the proportional factor K_{dry} over the surface and the corresponding induced offset in the thickness measurement. For this evaluation, the calibration frame at $100 \text{ } \mu\text{m}$ was used to compute the transmission of a flat film with constant thickness (a). A Gaussian low-pass filter was applied to extract the low frequency variation in K_{dry} (b). According to Eq. (4), we estimated the induced offset error on the film thickness (c) from the transmission (b). The offset between the two measurement techniques was measured by subtracting their time-averaged values (d). The patterns corresponding to the estimated and measured offsets are similar to each other; however, we notice a difference in amplitude in the offset range over the measuring field. The presence of the window might affect the estimation, and thus another

procedure should be found to correct for the spatial variation in K_{dry} in case of non-homogenous surfaces such as that of the LFS. We notice that the deviations visible in the time and spatial profile plots of Figs. 9 and 10 can be related to the measured offset deviation at the corresponding positions marked by green circles in Fig. 13d.

We calculated the standard deviation of the data presented in Fig. 13b over the measurement field to obtain a contribution of 6.8 % to the uncertainty on K_{dry} . Furthermore, the interval of confidence of 0.22 % given by the calibration and the error on the value of $i_{\text{dry,calib,corr}}$ (0.49 % due to the uncertainty on the glass refraction index and 0.53 % according to time average measurement with a reference surface) were added to obtain a total uncertainty of $6.8 \% + 0.22 \% + 0.49 \% + 0.53 \% = 8 \%$ on K_{dry} .

Non-homogeneity of the surface reflection In case of a non-uniformity of the reflective properties of the wall surface, a variation in the deflection of the optical path due to refraction at a curved or inclined surface leads to a small misalignment between calibration and measurement. In case of the validation measurements on the surface of the LFS, this is an effect of the electrode pattern. The electrodes of the sensor are gold-coated and separated by an insulating material. Both materials have different optical properties. For example, considering one measuring pixel, a measurement on a tilted surface taken from a metallic electrode surface will deviate more than expected when compared to a flat film in which light from metallic and insulating surfaces merges due to the deflection of the optical path. Two main aspects associated with non-flat films contribute to the uncertainty of the measured intensity i : (1) the film thickness and the angle of incidence as discussed previously and (2) the spatial non-homogeneities of the surface reflection intensity associated with a shift of the reflection position as shown in Fig. 14. Figure 14 shows qualitatively the increase in uncertainty for the detected intensity i with a tilted film surface when the wall surface shows a non-homogeneous reflection intensity as is the case with the LFS surface.

The standard deviation of the intensity fluctuations between adjacent pixels was calculated on a dry surface (Fig. 7a) and was found to be equal to 12 % of the average intensity. The fraction of the surface observed by one pixel which is shifted by refraction was calculated as a function of the film thickness for a maximal film surface angle of 20° . The shift for a 600- μm -thick film is equal to 51 μm , i.e., 8.5 % of the pixel width. The fraction obtained was then multiplied by the standard deviation in order to obtain a relative uncertainty which is proportional to the film thickness and which reaches 1.02 % at 600 μm .

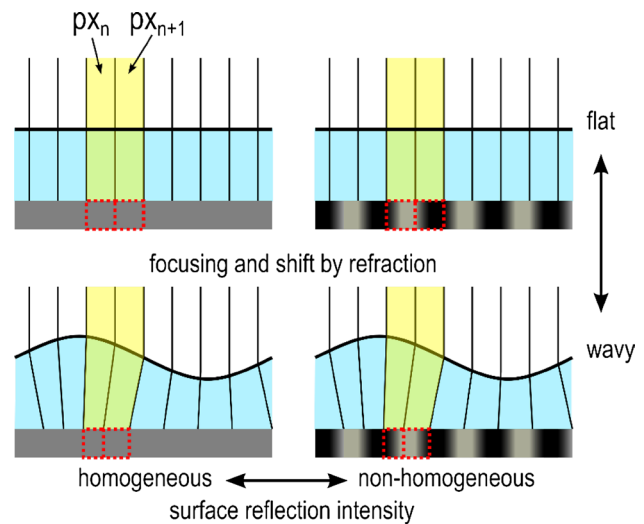


Fig. 14 Uncertainties related to the film surface angle (*left*) and non-homogenous optical properties of the wall surface (*right*). Two adjacent pixels were highlighted

Detection error The system gain of the NIR camera for the analog-to-digital conversion was measured at $12.36 \text{ e}^-/\text{DL}$ (electron per digital level). The camera's manufacturer guarantees an electronic noise smaller than 150 e^- RMS which has been verified experimentally. Due to the non-homogeneity of the surface reflection showing bright zones which would bring the detector to saturation, the supply voltage of the light source was adjusted such that only 7000 DL from a maximum of $2^{14} = 16,384$ DL was accounted in average over a dry surface. The resulting statistical error is 0.51 % for the intensity corresponding to a dry surface and raises to 0.65 and 1.1 % for film thicknesses of 100 and 600 μm , respectively.

Error propagation The estimated error on the parameters of Eq. (4) i , i_{dry} , K_{dry} , μ and c as described above was used to calculate the error propagation for different film thicknesses. The error on c given by the confidence of interval of the calibration was found to be 8.7 %. The total error on i is thickness dependent and corresponds to the sum of the uncertainties relative to the angle of incidence, the non-homogeneity of the surface reflection, the counting statistic of detection and the uncertainty bond to the relative measurement with a reference surface. Table 2 shows the propagation of errors for the parameters of Eq. (4).

The main source of error is related to the non-homogeneities of the surface optical properties. The uncertainty on K_{dry} creates an offset error whose relative value decreases with a growing film thickness. The electrodes affect the spatial homogeneity of the surface reflection intensity,

Table 2 Estimation and propagation of errors

Parameter	Error decomposition (%)					Error on x (μm)
	μ	K_{dry}	I	i_{dry}	C	
Thickness (μm)						
100	0.03	93.24	6.18	0.50	0.06	56.05
300	0.25	89.14	10.03	0.48	0.11	57.32
600	0.90	80.86	17.58	0.45	0.24	60.18

and the associated error on i has an increasing impact with growing film thickness. Note that this effect is much reduced on more homogeneous surfaces than the one of the LFS used for the direct comparison in this work. Also, such surfaces would allow for higher reflected intensities which would improve the statistical error of detection. Measurements on surfaces with finer grain structures which provide a homogeneous reflection should improve the measurement accuracy.

6 Conclusion

An imaging technique based on NIR light absorption for the two-dimensional mapping of water film thickness was developed and tested. The time-resolved liquid film thickness distribution over a 2D domain was recorded. We measured a free-falling water film on a vertical wall. The film was turbulent and isothermal. A calibration procedure, which can be applied to different types of wall surfaces, was elaborated. The camera provides detailed information on the flow pattern and its evolution in time. Synchronous independent measurements with an LFS demonstrated a good qualitative and quantitative agreement for isothermal films. The inhomogeneous surface of the LFS, consisting of gold-covered electrodes and darker insulating areas, caused the majority of the deviation between the measuring techniques. We assume that the application of the NIR imaging to other less inhomogeneous surfaces is less challenging.

In the future, we plan to extend the application of the technique to water films that do not cover the entire surface completely. The difference between the reflection of a dry and wet surface will be used for the detection of the presence of rivulets and droplets. Furthermore, we intend to measure the thickness of condensing and evaporating films in steam-rich atmospheres where particular attention should be paid to errors related to steam absorption and large temperature gradients in the film. In particular, we will explore the ability of the presented method, of relative measurements by means of a reference surface, to correct for fluctuations in absorption by larger vapor concentrations in the view path.

It is also planned to use the wavelength difference between narrowband NIR and the blackbody radiation for

a simultaneous mapping of film thickness and film surface temperature in case of vapor condensation in the presence of non-condensable gases by adding a second infrared camera sensible to mid- or far-infrared light.

Acknowledgments This work was conducted in the framework of the LINX project with the cooperation of IRSN and ENSI. The authors gratefully acknowledge those organizations for their financial support (H-100762) through which this work was made possible.

Appendix 1

On the side of the camera, the intensity $I_{\text{dry,max}}$ necessary to reach saturation of one sensitive area (pixel) on the focal plane array is expressed as follows:

$$I_{\text{dry,max}}(\lambda) = \frac{100\% \cdot \text{FWC}}{\eta_Q(\lambda) \cdot \Gamma_{\text{lens}}(\lambda)} \cdot \frac{E_Y(\lambda)}{T_i} \left[\frac{\text{J}}{\text{s}} \right] \tag{5}$$

The full well capacity (FWC) over the quantum efficiency η_Q is a design parameter of the detector, Γ_{lens} is the lens transmission, $E_Y(\lambda)$ is the photon energy for the specified wavelength λ , and T_i is the integration time.

On the side of the illumination, assuming a wall surface with Lambertian reflectance, $I_{\text{dry,max}}$ is related to the total amount of light falling on the wall surface I_{illu} as follows:

$$I_{\text{dry,max}} = \int_{\Omega_{\text{lens}}} I_{\Omega,\text{dry}} d\Omega \cong I_{\Omega,\text{dry},90^\circ} \cdot \Omega_{\text{lens}} = I_{\text{dry},90^\circ} \left[\frac{\text{J}}{\text{s}} \right] \tag{6}$$

$$I_{\text{dry,tot}}_{\text{lambertian}} = \int_0^{2\pi} \int_0^{\pi/2} I_{\Omega,\text{dry},90^\circ} \cos(\theta) \sin(\theta) d\varphi d\theta = I_{\Omega,\text{dry},90^\circ} \cdot \pi \left[\frac{\text{J}}{\text{s}} \right] \tag{7}$$

$$I_{\text{dry},90^\circ} = \frac{I_{\text{dry,tot}}}{\pi} \cdot \Omega_{\text{lens}} = I_{\text{illu}} \cdot \frac{S_{\text{FOV}}}{S_{\text{illu}}} \cdot \frac{1}{N_{\text{pix}}} \cdot \alpha \cdot \frac{\Omega_{\text{lens}}}{\pi} \left[\frac{\text{J}}{\text{s}} \right] \tag{8}$$

In Eq. (6), we assume a small solid angle covered by the lens's pupil Ω_{lens} such that the intensity of reflected light per unit of solid angle, $I_{\Omega,\text{dry}}$, in the integration domain, Ω_{lens} , is approximated as a constant equal to the

maximum reflection intensity, $I_{\Omega, \text{dry}, 90^\circ}$, normal to the surface. In Eq. (7), the factor π denotes the ratio between $I_{\Omega, \text{dry}, 90^\circ}$ and the total amount of reflected light, $I_{\text{dry}, \text{tot}}$, by a Lambertian radiator in all directions of the hemisphere. In Eq. (8), S_{illu} is the surface on the wall being illuminated, S_{FOV} is the surface corresponding to the FOV, N_{pix} is the number of pixels, and α is the surface albedo denoting the fraction of light being reflected. While the three first terms on the right side of Eq. (8) represent the illumination per pixel area in the FOV, the two last terms determine the fraction of light from one illuminated pixel which actually enters the camera’s lens. The solid angle, Ω_{lens} , is approximated as follows:

$$\Omega_{\text{lens}} \cong 4\pi \frac{S_{\text{lens}}}{S_{\text{sphere}}} = \frac{1}{4} \frac{\pi D^2}{L^2} = \frac{\pi}{4L^2} \cdot \left(\frac{f}{f/}\right)^2 \text{ [sr]} \tag{9}$$

where L is the distance between the wall and the camera and D is the diameter of the lens entrance pupil expressed in terms of the focal length, f , and relative aperture $f/$.

The overall illumination of the wall surface, I_{illu} , is related to the electrical power of a light projection system as follows:

$$I_{\text{illu}}(\lambda, \text{BW}) = P_{\text{ele}} \cdot \eta_{\text{source}} \cdot C_{\text{geo}} \cdot \eta_{\text{opt}} \left[\frac{\text{J}}{\text{s}} \right] \tag{10}$$

where P_{ele} is the applied electric power and η_{source} is the light source efficiency which describes its ability to convert electrical power into light with specific wavelength and band-pass. The geometrical collection ratio, C_{geo} , is the fraction of light collected by the condenser lens and the rear mirror (see Fig. 3) and is given by the solid angle they cover around the bulb. The dimensionless number, η_{opt} , is the optical efficiency or quality of the light projection system and corresponds to the fraction of collected light transmitted through the optical elements which contributes to the illumination.

In order to estimate P_{ele} , we assume that the incandescent filament behaves like a blackbody with homogenous temperature and that the electrical power is entirely converted into heat by the joule effect in the filament. Convective heat transfer in the lamp is neglected. The maximum light source efficiency, $\eta_{\text{source}, \text{max}}$, obtained with filtered blackbody emission in a band-pass centered at the observation wavelength, λ_{obs} , is found according to the Wien’s displacement law for the optimized temperature: $T_{\text{opt}} = b/\lambda_{\text{max}} = b/\lambda_{\text{obs}}$. The wavelength λ_{max} corresponds to the maximum of the emission spectrum, and b is the Wien’s displacement constant. The value of $\eta_{\text{source}, \text{max}}$ is calculated using Planck’s law and its integrated form: the Stefan–Boltzmann law at wavelength $\lambda_{\text{obs}} = \lambda_{\text{max}}$. For a narrowband filter with the band-pass width W , the following approximation is derived.

$$\eta_{\text{source}, \text{max}} = \frac{I_{\text{BB}, W}}{I_{\text{BB}, \text{tot}}} \cong \frac{\pi \cdot \frac{2hc^2}{\lambda_{\text{obs}}^5} \cdot \frac{1}{e^{hc/\lambda k_B T_{\text{opt}}(\lambda_{\text{obs}})} - 1} \cdot W}{\sigma T_{\text{opt}}(\lambda_{\text{obs}})^4} \tag{11}$$

where $I_{\text{BB}, W}$ and $I_{\text{BB}, \text{tot}}$ denote the blackbody emission in the band-pass and for the full spectrum h is the Planck’s constant, c is the speed of light, σ is the Stefan–Boltzmann constant, and k_B is the Boltzmann constant. The light source efficiency for the non-filtered light passing through the BK7 elements $\eta_{\text{source}, \text{BK7}}$ was evaluated by the ratio between the integrated blackbody emission over the 300–2700 nm BK7 transmission range and the total blackbody emission $I_{\text{BB}, \text{tot}}$.

Equations (A1)–(A7) were used to estimate the size of the halogen bulb and the radiation flux reaching the surface. Table 3 lists the values of the parameters and the estimations obtained according to the experimental setup used in our work.

Appendix 2

We define a reflection loss factor at an interface from the medium x to the medium y as follows:

$$L_{R, x \rightarrow y} = (1 - R_{x \rightarrow y})$$

L characterizes the decrease in intensity due to the reflected share R of the incoming radiation. According to Snell’s law and Fresnel equations, the following relation applies for a bidirectional optical path as shown in Fig. 2:

$$L_{R, x \rightarrow y} = L_{R, y \rightarrow x}$$

The total attenuation along the optical path connecting a pixel of the camera with the light source (pixel indices omitted) contains reflection losses at the air–water ($a \rightarrow w$) interface, the reflection efficiency of the wet wall R_{wet} , and the absorption in the water film and in the air between measuring setup and wall. During the measurement, the brightness is proportional to:

$$\begin{aligned} I(x_w) &= I_{\text{na}} \cdot e^{-\mu_a x_a} \cdot L_{R, a \rightarrow w} \cdot e^{-\mu_w x_w} \cdot R_{\text{wet}} \\ &\quad \cdot e^{-\mu_w x_w} \cdot L_{R, w \rightarrow a} \cdot e^{-\mu_a x_a} \\ &= I_{\text{na}} \cdot L_{R, a \rightarrow w}^2 \cdot R_{\text{wet}} \cdot e^{-2\mu_w x_w} \cdot e^{-2\mu_a x_a} \end{aligned}$$

Here, I_{na} is the intensity of the non-attenuated beam. The calibration has to provide values of I_{na} , $L_{R, a \rightarrow w}$, R_{wet} , μ_w , $A_{\text{air}} = \exp(-2\mu_a x_a)$ or to allow canceling out some of the unknowns. If a window is placed in front of the optical assembly, the reflection and absorption by the glass can be treated in the same way.

In the dry case:

$$I_{\text{dry}} = I_{\text{na}} \cdot R_{\text{dry}} \cdot e^{-2\mu_a x_a}$$

Table 3 Parameters and estimations for the design of a light projection system with halogen bulb

Parameter	Value	Estimation	Value
FWC	1.75×10^5	$I_{\text{dry,max}}$ (W)	8.8×10^{-11}
λ_{obs} (m)	1612×10^{-9}	Ω_{lens} (sr)	4.9×10^{-4}
W (m)	32×10^{-9}	I_{illu} (W)	0.12
N_{pix}	81,920	P_{ele} (W)	102
$S_{\text{FOV}}/S_{\text{illu}}$	~0.48	$\eta_{\text{source,max}}$	1.3×10^{-2}
α	~0.8	$\eta_{\text{source,BK7}}$	0.62
L (m)	1	Surface radiation flux (W m ⁻²) (with narrowband filter)	2
η_Q	0.7		
T_i (s)	5×10^{-4}		
T_{lens}	0.75		
f/l	2	Surface radiation flux (W m ⁻²) (no filter expect N-BK7 glass)	92
f (m)	0.05		
C_{geo}	0.15		
η_{opt}	~0.6		
S_{FOV} (m ²)	3×10^{-2}		

The symbol ‘~’ denotes approximated parameters

In the wet calibration case with glass:

$$I_{\text{calib}}(x_w) = I_{\text{na}} \cdot L_{R,a \rightarrow g}^2 \cdot L_{R,g \rightarrow w}^2 \cdot e^{-2\mu_g x_g} \cdot R_{\text{wet}} \cdot e^{-2\mu_w x_w} \cdot e^{-2\mu_a x_a}$$

For the dry calibration case with glass window:

$$I_{\text{calib,dry}} = I_{\text{na}} \cdot L_{R,a \rightarrow g}^4 \cdot e^{-2\mu_g x_g} \cdot R_{\text{dry}} \cdot e^{-2\mu_a x_a}$$

We introduce a reference surface and assume that the absorption by air along the optical path between camera and reference surface is a good approximation of the absorption by the air on the optical path of every camera pixel in the measuring domain:

$$I_{\text{ref}} = I_{\text{na,ref}} \cdot R_{\text{ref}} \cdot e^{-2\mu_{a,\text{ref}} x_{a,\text{ref}}} \cong I_{\text{na,ref}} \cdot R_{\text{ref}} \cdot e^{-2\mu_a x_a}$$

All recorded intensities, regardless of whether during the measurement or during calibration, are related to the reference intensity. In this way, the changes in absorption by the air, e.g., due to moisture variations, cancel out with the accuracy of the assumption that the absorption in the air is similar for both optical paths:

$$i(x_w) = \frac{I(x_w)}{I_{\text{ref}}} = \frac{I_{\text{na}}}{I_{\text{na,ref}} \cdot R_{\text{ref}}} \cdot L_{R,a \rightarrow w}^2 \cdot R_{\text{wet}} \cdot e^{-2\mu_w x_w}$$

The quotient $i_{\text{na}}^* = \frac{I_{\text{na}}}{I_{\text{na,ref}} \cdot R_{\text{ref}}}$ is a constant. Variations in the illumination intensity or in the quantum efficiency of the detector due to temperature changes have the same effect on I_{na} and $I_{\text{na,ref}}$ and thus cancel out through the division when i is computed. It can be used as a dimensionless reference intensity, in which air absorption cancels out:

$$i(x_w) = i_{\text{na}}^* \cdot L_{R,a \rightarrow w}^2 \cdot R_{\text{wet}} \cdot e^{-2\mu_w x_w} \tag{12}$$

$$i_{\text{dry}} = \frac{I_{\text{dry}}}{I_{\text{ref}}} = i_{\text{na}}^* \cdot R_{\text{dry}} \tag{13}$$

$$i_{\text{calib}}(x_w) = \frac{I_{\text{calib}}(x_w)}{I_{\text{ref,calib}}} = i_{\text{na,calib}}^* \cdot L_{R,a \rightarrow g}^2 \cdot L_{R,g \rightarrow w}^2 \cdot e^{-2\mu_g x_g} \cdot R_{\text{wet}} \cdot e^{-2\mu_w x_w} \tag{14}$$

$$i_{\text{calib,dry}} = \frac{I_{\text{calib,dry}}}{I_{\text{ref,calib}}} = i_{\text{na,calib}}^* \cdot L_{R,a \rightarrow g}^4 \cdot e^{-2\mu_g x_g} \cdot R_{\text{dry}} \tag{15}$$

In our experiment, the reference surface was identical for the calibration and the measurements such that $I_{\text{ref,calib}} = i_{\text{ref}}$. Here, we treat the general case where two different reference surfaces are used. The effect of the glass window used during calibration can be quantified by relating i to i_{dry} and i_{calib} to $i_{\text{calib,dry}}$:

$$\frac{i(x_w)}{i_{\text{dry}}} = \frac{R_{\text{wet}}}{R_{\text{dry}}} \cdot L_{R,a \rightarrow w}^2 \cdot e^{-2\mu_w x_w}$$

$$\frac{i_{\text{calib}}(x_w)}{i_{\text{calib,dry}}} = \frac{R_{\text{wet}}}{R_{\text{dry}}} \cdot \frac{L_{R,g \rightarrow w}^2}{L_{R,a \rightarrow g}^2} \cdot e^{-2\mu_w x_w}$$

To characterize the intensity step change between a wet and a dry surface, we define the correction factor K_{dry} as:

$$K_{\text{dry}} = \frac{i(x_w \rightarrow 0)}{i_{\text{dry}}} = \frac{R_{\text{wet}}}{R_{\text{dry}}} \cdot L_{R,a \rightarrow w}^2$$

This yields:

$$\frac{i(x_w)}{i_{\text{dry}}} = K_{\text{dry}} \cdot e^{-2\mu_w x_w}$$

$$\frac{i_{\text{calib}}(x_w)}{i_{\text{calib,dry}}} = K_{\text{dry}} \frac{L_{R,g \rightarrow w}^2}{L_{R,a \rightarrow g}^2 \cdot L_{R,a \rightarrow w}^2} \cdot e^{-2\mu_w x_w}$$

We further define the corrected dry measurement in the presence of a window $i_{\text{calib,dry,corr}}$ as;

$$i_{\text{calib,dry,corr}} = i_{\text{calib,dry}} \frac{L_{R,a \rightarrow g}^2 \cdot L_{R,a \rightarrow w}^2}{L_{R,g \rightarrow w}^2} \tag{16}$$

The reflection losses were calculated according to the refraction indexes of air, water and glass.

$$\frac{i(x_w)}{i_{\text{dry}}} = \frac{i_{\text{calib}}(x_w)}{i_{\text{calib,dry,corr}}} = K_{\text{dry}} \cdot e^{-2\mu_w x_w} \tag{17}$$

Fitting an exponential function to the calibration data obtained for different water layers between glass and wall surface gives the constants K_{dry} and $2\mu_w$.

Applying Eq. (16), we observed a systematic overestimation of the film thickness when comparing temporally and spatially averaged measurements with the LFS. Thus, Eq. (16) leads to an underestimation of $i_{\text{dry,calib,corr}}$. In order to calculate the right value of $i_{\text{dry,calib,corr}}$, we consider the contribution of internal reflections contributing to the overall illumination. In fact, the second series of reflections when the light escapes from the wall surface is not lost since it is reflected back on the same surface and thus contributes to the total illumination. In the limit of infinitely thin films ($x_w \rightarrow 0$), the backward reflected light is not attenuated in the water film. With the assumption of a surface albedo equal to 1, we do not consider the second series of reflections as losses such that:

$$i'(x_w \rightarrow 0) = i_{\text{na}}^* \cdot L_{R,a \rightarrow w} \cdot R_{\text{wet}} \tag{18}$$

$$i'_{\text{calib}}(x_w \rightarrow 0) = i_{\text{na}}^* \cdot L_{R,a \rightarrow g} \cdot L_{R,g \rightarrow w} \cdot e^{-2\mu_g x_g} \cdot R_{\text{wet}} \tag{19}$$

$$i'_{\text{calib,dry}} = i_{\text{na}}^* \cdot L_{R,a \rightarrow g}^2 \cdot e^{-2\mu_g x_g} \cdot R_{\text{dry}} \tag{20}$$

This yields:

$$i'_{\text{calib,dry,corr}} = i'_{\text{calib,dry}} \frac{L_{R,a \rightarrow g} \cdot L_{R,a \rightarrow w}}{L_{R,g \rightarrow w}} \tag{21}$$

Using Eq. (21), where the reflection losses are not squared, results in well-matching average values with both techniques. While Eqs. (B7–B8) are valid for infinitely thin films, Eqs. (B1–B4) are valid in the limit of infinitely thick films where the second series of reflections are completely lost by absorption in the film.

For the purpose of the measurement, we use the following approximation.

$$\frac{i'(x_w)}{i_{\text{dry}}} \cdot \frac{i'_{\text{calib}}(x_w)}{i'_{\text{calib,dry,corr}}} \cdot K'_{\text{dry}} \cdot e^{-2\mu'_w x_w} \tag{22}$$

where μ'_w is an apparent absorption coefficient, where $\mu'_w > \mu_w$ according to the extended absorption path followed by multiple internal reflections. The good fit of the calibration data justifies the use of this approximation. For simplification, we further refer to $x, i, i_{\text{dry}}, K_{\text{dry}}$ and μ instead of $x_w, i', i'_{\text{dry}}, K'_{\text{dry}}, \mu'_w$.

Appendix 3

Light refraction and reflection associated with the tilt angle θ_i of the water film surface induce additional intensity losses. The intensity I deviates from the Beer–Lambert law as follows:

$$I(x, \theta_i, n_1, n_2) = I_0 \cdot e^{-\mu \cdot x'(x, \theta_i, n_1, n_2)} \cdot f(\theta_i, n_1, n_2) \tag{23}$$

$$\frac{I(x, \theta_i, n_1, n_2)}{I(x, \theta_i = 0, n_1, n_2)} = e^{-\mu \cdot (x'(x, \theta_i, n_1, n_2) - 2 \cdot x)}$$

$$\frac{f(\theta_i, n_1, n_2)}{f(\theta_i = 0, n_1, n_2)} \tag{24}$$

$$x'(x, \theta_i, n_1, n_2) = \frac{2 \cdot x}{\cos(\theta_i - \theta_t(\theta_i, n_1, n_2))} \tag{25}$$

$$f(\theta_i, n_1, n_2) = L_{R,a \rightarrow w}^2(\theta_i, n_1, n_2) \cdot R_D(\theta_i, n_1, n_2) \tag{26}$$

where Eq. (24) corresponds to the deviation compared with a flat film as depicted in Fig. 11. Equation (C3) characterizes the increased length of the absorption path according to the refraction of light where x' is the absorption path length, x is the film thickness, and θ_t is the transmitted angle as shown in Fig. 2. The refraction indexes $n_1 = 1$ and $n_2 = 1.31$, in the gaseous and the liquid phase, respectively, are constant. The function f derived in Eq. (26) expresses further intensity losses in the film surface transmission $L_{R,a \rightarrow w}$ and in the diffuse reflection coefficient R_D of the wall surface. The angle $(\theta_i - \theta_t)$ is formed between the incident light falling on the wall surface and the wall normal direction. The two terms in Eq. (26) as well as the denominator in Eq. (25) take values between 0 and 1, which leads to an attenuation of the overall transmission when compared to the Beer–Lambert law. The values of θ_t and $L_{R,a \rightarrow w}^2$ are derived from Snell’s law and the Fresnel’s equations, respectively. The factor 2 in the numerator of Eq. (25) and the square function in Eq. (27) represent the fact that absorption and reflection losses happen twice.

Under the assumption of a surface with ideal diffuse reflection, as described by the Lambert’s cosine, law R_D is expressed as follows:

$$R_D(\theta_i, n_1, n_2) = R_{\text{wet}} \cos(\theta_i - \theta_t(\theta_i, n_1, n_2)) \tag{27}$$

The reflection efficiency of the wet wall R_{wet} cancels out through the division in Eq. (24).

References

- Alekseenko SV, Antipin VA, Cherdantsev AV, Kharlamov SM, Markovich DM (2008) Investigation of waves interaction in annular gas–liquid flow using high-speed fluorescent visualization technique. *Microgravity Sci Technol* 20(3–4):271–275
- Ambrosini W, Forgione N, Oriolo F (2002) Statistical characteristics of a water film falling down a flat plate at different inclinations and temperatures. *Int J Multiph Flow* 28(9):1521–1540
- Anderson MH, Herranz LE, Corradini ML (1998) Experimental analysis of heat transfer within the AP600 containment under postulated accident conditions. *Nucl Eng Des* 185(2–3):153–172
- Belt R, Van't Westende J, Portela L, Prasser H-M, Mudde R, Olie-mans R (2007) Interfacial waves and shear-stress in vertical upward annular flow. In: *Proceedings of the sixth international conference on multiphase flow*, Leipzig, Germany
- Belt R, Van't Westende J, Prasser H-M, Portela L (2010) Time and spatially resolved measurements of interfacial waves in vertical annular flow. *Int J Multiph Flow* 36(7):570–587
- Bieberle M, Schleicher E, Fischer F, Koch D, Menz H-J, Mayer H-G, Hampel U (2010) Dual-plane ultrafast limited-angle electron beam X-ray tomography. *Flow Meas Instrum* 21(3):233–239
- Brissinger D, Parent G, Boulet P (2014) Experimental study on radiation attenuation by a water film. *J Quant Spectrosc Radiat Transfer* 145:160–168
- Chen ZQ, Hermanson JC, Shear MA, Pedersen PC (2005) Ultrasonic monitoring of interfacial motion of condensing and non-condensing liquid films. *Flow Meas Instrum* 16(6):353–364
- Clark WW (2002a) Liquid film thickness measurement. *Multiph Sci Technol* 14(1):1–74
- Clark W (2002b) The interfacial characteristics of interfacial falling film reactors. PhD Thesis, Nottingham
- Clegg AJ (1969) Studies of film flow on wetted wall columns, PhD Thesis. University of Surrey, Guildford
- Corkill JM, Goodman JF, Ogden CP, Tate JR (1963) The structure and stability of black foam films. *Proc R Soc A* 273(1352):84–102
- da Silva M, Sühnel T, Schleicher E, Vaibar R, Lucas D, Hampel U (2007) Planar array sensor for high-speed component distribution imaging in fluid flow applications. *Sensors* 7:2430–2445
- da Silva M, Lu Y, Sühnel T, Schleicher E, Thiele S, Kernchen R, Diele K-H, Hampel U (2008) Autonomous planar conductivity array sensor for fast liquid distribution imaging in a fluid coupling. *Sens Actuators A* 147:508–515
- Damsohn M (2011) Liquid films and droplet deposition in a BWR fuel element. ETH Zürich, Zürich
- Damsohn M, Prasser H-M (2009) High-speed liquid film sensor for two-phase flows with high spatial resolution based on electrical conductance. *Flow Meas Instrum* 20(1):1–14
- de la Rosa JC, Escrivá A, Herranz LE, Cicero T, Muñoz-Cobo JL (2009) Review on condensation on the containment structures. *Prog Nucl Energy* 51(1):32–66
- Debrégeas G, Martin P, Brochard-Wyart F (1995) Viscous bursting of suspended films. *Phys Rev Lett* 75(21):3886–3889
- Doniec A (1988) Flow of a laminar liquid film down a vertical surface. *Chem Eng Sci* 43(4):847–854
- Dumin DJ (1967) Measurement of film thickness using infrared interference. *Rev Sci Instrum* 38(8):1107–1109
- Fischer F, Hampel U (2010) Ultra fast electron beam X-ray computed tomography for two-phase flow measurement. *Nucl Eng Des* 240(9):2254–2259
- Greszik D, Yang H, Dreier T, Schulz C (2011) Measurement of water film thickness by laser-induced fluorescence and Raman imaging. *Appl Phys B* 102(1):123–132
- Hampel U, Speck M, Koch D, Menz H-J, Mayer H-G, Fietz J, Hoppe D, Schleicher E, Zippe C, Prasser H-M (2005) Experimental ultra fast X-ray computed tomography with a linearly scanned electron beam source. *Flow Meas Instrum* 16(2–3):65–72
- Huang X, Cheng X (2014) Simulation of PWR's passive containment cooling with an advanced water film model. In: *Proceedings of ICAPP*, Charlotte
- Incropera FP, DeWitt DP (1996) Fundamentals of heat and mass transfer. In: *Empirical correlation: external free convection flows*. Wiley, New York, pp 492–505. ISBN: 0-471-30460-3
- Kamei T, Serizawa A (1998) Measurement of 2-dimensional local instantaneous liquid film thickness around simulated nuclear fuel rod by ultrasonic transmission technique. *Nucl Eng Des* 184(2–3):349–362
- Kang HC, Kim MH (1992) Measurement of three-dimensional wave form and interfacial area in an air–water stratified flow. *Nucl Eng Des* 136(3):347–360
- Kickhofel JL, Zboray R, Damsohn M, Kaestner A, Lehmann EH, Prasser H-M, Kaestner A, Lehmann EH, Prasser H-M (2011) Cold neutron tomography of annular coolant flow in a double subchannel model of a boiling water reactor. *Nucl Instrum Methods Phys Res, Sect A* 651(1):297–304
- Kofman N, Mergui S, Ruyter-Quil C (2014) Three-dimensional instabilities of quasi-solitary waves in a falling liquid film. *J Fluid Mech* 757:854–887
- Kou L, Labrie D, Chylek P (1993) Refractive indices of water and ice in the 0.65–2.5 μm spectral range. *Appl Opt* 32(19):3531–3540
- Malet J, Porcheron E, Vendel J (2005) Filmwise condensation applied to containment studies: conclusions of the TOSQAN air–steam condensation tests. In: *NURETH-11—11th international topical meeting on nuclear reactor thermal-hydraulics*. Avignon
- Ozler Emrah Talip (2007) Modelling of dropwise condensation on a cylindrical surface including the sweeping effect. M.S. Thesis, Middle East Technical University, Ankara
- Sattelmayer T, Sill K, Wittig S (1987) Optisches Messgerät zur Bestimmung der eigenschaften welliger Flüssigkeitsfilme. *Tech Mess* 4(54):155–160
- Segelstein DJ (1981) The complex refractive index of water. M. S. Thesis, University of Missouri-Kansas City, Kansas City
- The HITRAN 2012 (2013) Molecular spectroscopic database. *J Quant Spectrosc Radiat Transfer* 130:4–50
- Twomey SA, Bohren CF, Mergenthaler JL (1986) Reflectance and albedo differences between wet and dry surfaces. *Appl Opt* 25(3):431–437
- Wieliczka DM, Weng S, Query MR (1989) Wedge shaped cell for highly absorbent liquids: infrared optical constants of water. *Appl Opt* 28(9):1714–1719
- Wittig S, Himmelsbach J, Noll B, Feld HJ, Samenink W (1992) Motion and evaporation of shear-driven liquid films in turbulent gases. *J Eng Gas Turbines Power* 114(2):395–400
- Wolff LB (1994) Diffuse-reflectance model for smooth dielectric surfaces. *Opt Soc Am* 11(11):2956–2968
- Xu G, Tazawa M, Jin P, Yoshimura K (2003) Diffuse reflection of ceramics coated with dielectric thin films. *Appl Opt* 42(7):1352–1359
- Yang H, Greszik D, Dreier T, Schulz C (2010) Simultaneous measurement of liquid water film thickness and vapor temperature using near-infrared tunable diode laser spectroscopy. *Appl Phys B, Duisburg*, pp 385–390
- Yang H, Greszik D, Wlokas I, Dreier T, Schultz C (2011) Tunable diode laser absorption sensor for the simultaneous measurement of water film thickness, liquid- and vapor-phase temperature. *Appl Phys B* 104(1):21–27
- Yu Y, Wei S, Yang Y, Cheng X (2011) Experimental study of water film falling and spreading on a large vertical plate. *Prog Nucl Energy* 54:22–28